Engineering Structures 327 (2025) 119623

Contents lists available at ScienceDirect

Engineering Structures

journal homepage: www.elsevier.com/locate/engstruct

Multiphysical simulation of iron-based shape memory alloy (Fe-SMA) activation embedded in concrete structures

Ali Saeedi [a], Alireza Tabrizikahou [b], Paul-Remo Wagner [c], Moslem Shahverdi [a,d],*

[a] Empa, Swiss Federal Laboratories for Materials Science and Technology, Dübendorf, 8600, Switzerland
[b] Institute of Building Engineering, Poznań University of Technology, Piotrowo 5, 60-965, Poznań, Poland
[c] Matrisk GmbH, Alte Obfelderstrasse 50, Affoltern am Albis, 8910, Zurich, Switzerland
[d] School of Civil Engineering, University of Tehran, 16th Azar Street, Tehran, Iran

ARTICLE INFO

Keywords:
Iron based shape memory alloy (Fe-SMA)
Concrete beams
Multiphysical simulation
Activation process
Pre-stressing

ABSTRACT

Shape memory alloys (SMAs) are a well-known type of smart material that recovers its original shapes upon activation. This unique property makes SMAs attractive for pre-stressing applications in civil engineering. Iron-based SMAs (Fe-SMAs) are particularly promising for civil engineering applications because of their low cost, high stiffness, and large recovery force generation. The activation of Fe-SMAs embedded in concrete involves four main physical processes: electrical current flow, heat generation and transfer, stress generation, and phase transformation. A multiphysical simulation of the Fe-SMA activation is performed in the present study, considering the interaction of the involved physical models. The verification of the model is done in multiple steps, by comparing the simulation results with the available experimental results on Fe-SMA activation. Following the model verification, a parametric study is done to investigate the effective activation, and geometrical parameters on the heat, and stress distributions. The model provides a reliable tool for understanding the behavior of the embedded Fe-SMA reinforcement and surrounding concrete during activation. It also aids in designing the appropriate activation and geometrical parameters for SMA-reinforced concrete structures, based on the required mechanical properties of the structure.

1. Introduction

Shape memory alloys (SMAs), a well-known type of metallic smart material, are renowned for their ability to remember and recover their initial shape after deformation through external stimuli such as heat [1,2]. As one of their main characteristics, the shape memory effect (SME) results from a reversible martensitic phase transformation that appears in the alloy at particular threshold temperatures [3]. Their other unique feature is superelasticity which allows the SMAs to experience substantial reversible strains when loaded and unloaded at temperatures above the phase-transformation range (i.e., the austenite finish temperature A_f) [4]. Because of their unique mechanical and physical properties, SMAs have been widely used in various fields of applications [5,6]. In recent years, SMAs have received considerable interest in civil engineering applications, particularly in earthquake resistance and the retrofitting of existing buildings and bridges [7]. Using Fe-SMA in earthquake-resistant buildings can reduce deformation and floor acceleration demands, leading to a lower probability of collapse [8,9], provide excellent recentering abilities and moderate energy dissipation [10], and enable connection recentering with supplementary energy dissipation in structural connections [11]. They can enhance the performance and durability of civil structures by providing capabilities such as pre-stressing [12–18], energy dissipation [19–21], self-centering [22,23], and self-healing [24–26]. Among different types of SMAs, Iron-based SMAs (Fe-SMAs) are expected to have tremendous potential for civil engineering applications because of their high stiffness and low cost compared to the more expensive nickel-titanium (Ni–Ti) SMAs [18,27].

Multiphysics modeling is a simulation technique that integrates multiple physical phenomena and their interactions into a single computational model [28]. This approach allows for a more comprehensive analysis of complex systems by capturing the interplay between various physical fields, such as electromagnetic, thermal, mechanical, and fluid dynamics [29,30]. Since its inception, advancements in computer technology and interdisciplinary research have significantly expanded the scope and capabilities of multiphysics modeling, making it an essential tool in fields ranging from engineering to materials science [31].

The activation of Fe-SMAs embedded in concrete is a multiphysics process involving four major physical processes: electrical current flow,

* Corresponding author at: Empa, Swiss Federal Laboratories for Materials Science and Technology, Dübendorf, 8600, Switzerland.
E-mail address: moslem.shahverdi@empa.ch (M. Shahverdi).

https://doi.org/10.1016/j.engstruct.2025.119623
Received 12 August 2024; Received in revised form 11 November 2024; Accepted 2 January 2025
Available online 11 January 2025

heat transfer, continuum mechanics, and martensitic phase transformation [32–34]. An electrical current circulates through the SMA wires upon activation to heat the SMA (based on the electrical resistivity) and induce a reversible martensitic phase transformation, leading to a shape-recovery phenomenon [35]. This method can be utilized to strengthen concrete structures by implementing Fe-SMA wires or bars in concrete and activating them when necessary [36,37].

Multiphysical simulation is a powerful method for analyzing multiple domains, which integrates different physical models and numerical techniques into a unified computational platform [38–40]. In recent years, there has been considerable research and development undertaken regarding multiphysical simulations of SMA materials [41–44]. However, based on the available literature, the multiphysical studies on the activation process of Fe-SMAs in structures are very limited [45–47]. A recent study [47] utilized a multiphysical model to predict temperature distribution and pre-stress in Fe-SMA during its activation within concrete. Based on the findings, an activation guideline for Fe-SMAs embedded in concrete was established. Rodino and Maletta [45] employed a multiphysics model to capture the coupled thermo-mechanical response of SMA activation in a polymeric matrix. They reported excellent agreement between experimental and simulation results and presented an optimal activation configuration using a parametric study. In a recent study, Saeedi et al. [46] employed a multiphysics model to simulate the activation process of SMA actuators in a bi-stable shape-changing system. They used the simulation results to control the heating process, ensuring that the SMA does not overheat and achieves the desired shape change during activation.

The present study aims to establish a multiphysical macroscopic simulation of the interaction between the individual constituents of concrete with embedded Fe-SMA elements during the activation procedure to address the lack of accurate computational methods for comprehending the activation of Fe-SMAs embedded in concrete. The simulation is performed using Comsol software, which provides a framework for addressing the multiphysical aspects of the study. The Lagoudas model [48] is used to simulate the SMA material behavior. However, because this model was originally developed for Ni–Ti SMA materials, adjustments were made to the formulation to adapt it to Fe-SMAs. In this regard, the formulation of material characterization was modified by adding the nonlinear strain components. The simulation results were assessed and compared with the results of previous experiments.

The main contribution of the present study is the development of a comprehensive multiphysical model for the activation of Fe-SMA in concrete. The simulation incorporates not only the temperature distribution within the system, but also the generated stress and strain field within the model during the activation phase. While the focus of the previous studies on Fe-SMA multiphysics simulations was mainly on temperature distribution upon activation, this study takes a broader approach by integrating a constitutive model of Fe-SMA to efficiently calculate the stress distribution in the Fe-SMA and the system. The present study offers an expanded multiphysics perspective on the Fe-SMA and concrete material system, providing deeper insights into the behavior of Fe-SMA during activation. Using the multiphysics model helps to understand the activation behavior and extract additional data from the experiment. Additionally, it can be used to define proper SMA mechanical and activation parameters prior to the fabrication of the specimen. The required pre-strain level, the volume fraction of SMA, and the required temperature and current (in the case of resistive heating) can be obtained using the model. This study emphasizes the importance of developing reliable simulation tools to understand the behavior of Fe-SMA embedded in concrete during activation. Such simulation approaches and tools can promote the application of Fe-SMAs in different engineering fields, particularly in civil engineering.

2. Multiphysical modeling

Multiphysics modeling of SMA actuation embedded in a concrete structure requires considering the interaction between the involved physical phenomena. For the activation process, the main steps are heat generation in the Fe-SMA due to its electrical resistance, transferring the generated heat to the surrounding materials (concrete and air), and stress transfer between embedded Fe-SMA and host concrete structure. The goal of the present work is to examine the stress distribution inside the SMA and concrete materials, as well as the resulting beam displacement.

In the modeling process, two different multiphysics simulation approaches are employed to accurately model the interactions between thermal and mechanical behaviors within the Fe-SMA and concrete composite system.

Thermal expansion multiphysics is employed to capture the effects of temperature changes in the Fe-SMA on the mechanical stresses. Thermal conductivity between the SMA and concrete is modeled to account for heat flow within the composite system and convection on the outer sides of the concrete specimen is incorporated to simulate heat transfer with surrounding air. For thermal expansion, the secant coefficient of thermal expansion is employed to determine the thermal strains:

$$\varepsilon_{\mathrm{th}} = \alpha \left(T - T_{\mathrm{ref}}\right), \tag{1}$$

where $\varepsilon_{\mathrm{th}}$ is the thermal strain due to change in temperature, and α is the secant coefficient of thermal expansion. The temperature (T), on the other hand, is calculated by considering resistive heating in the Fe-SMA.

Resistive heating during activation is modeled by simulating electric current flow and incorporating the Joule heating effect into the thermal analysis. The two modules—electric current and heat transfer in solids—are linked together through an electromagnetic heating multiphysics module to simulate heat generation and transfer during the activation of the Fe-SMA reinforcements.

Initially, the electric current flowing through the Fe-SMA reinforcement is modeled using the principles of electrical conduction:

$$J = \sigma E + J_{\mathrm{e}}, \tag{2}$$

where J is the current density, σ is the electrical conductivity of the Fe-SMA, E is the electric field, and J_{e} is externally generated current density.

The current density is utilized in the subsequent step to calculate Joule heating. The generated heat (Q_{e}) in the SMA due to electric current is determined by:

$$Q_{\mathrm{e}} = J \cdot E, \tag{3}$$

The generated heat, taking into account heat transfer within the SMA and between the SMA and concrete, results in a temperature rise in the model. The multiphysics coupling equation for electromagnetic heating is:

$$\rho C_{\mathrm{p}} \frac{\partial T}{\partial t} - \nabla \cdot (k \nabla T) = Q_{\mathrm{e}}, \tag{4}$$

where ρ is the density of the Fe-SMA and C_{p} its specific heat capacity. k represents the thermal conductivity, and Q_{e} the volumetric heat generation from Joule heating.

2.1. Setting up the models

With the target of simulating the activation process of Fe-SMA reinforcement embedded in concrete beams, three models were considered. For each of the three introduced models, the geometry of Fe-SMA reinforcements and boundary and loading conditions were selected similar to the experiments:

Model I: To verify the nonlinear material model for the Fe-SMA, the stress–strain behaviors of the Fe-SMA bar during loading and unloading were studied. For this model, the SMA bar with a diameter of 12 mm was modeled using the 2D axisymmetric method. The quadratic function was selected as the transformation function of SMA, and the modified shape memory material model was assigned to the geometry. The plastic strains were applied to the model as the external strains. Thermal expansions for martensite and austenite phases were also coupled to the model. The external strength was applied to one end while the other end was fixed.

Model II: Having verified the material model for the Fe-SMA, the activation of constrained Fe-SMA in the air was simulated using a multiphysical model. After verifying the nonlinear behavior of Fe-SMA in loading cycles, a simulation of Fe-SMA activation in air was first conducted to verify the model in a simpler context before moving on to the more complex simulation of Fe-SMA embedded in concrete. Experimental results were used to verify this model as well. A material model similar to Model I was also used for Model II. The geometry of the model was a strip with a thickness of 1.9 mm and a width of 14 mm. A fixed boundary condition was applied to the ends of the specimen. The time-dependent temperature was applied to the specimen based on the measured temperature during the experiment. The stress-temperature diagram was then obtained as the main result of the simulation.

Model III: Finally, the activation of Fe-SMA in concrete was studied, focusing on the interaction between the Fe-SMA and the surrounding concrete. This model was also verified using experimental results. In model III, the dimensions of the concrete beam were 50 mm × 35 mm × 700 mm, reinforced with an SMA strip with a cross-section of 1.5 mm × 15.97 mm. The same material model as Model II was used for the SMA reinforcement. The interface between the SMA and concrete was assumed to have perfect contact with no debonding. For the boundary conditions during the activation, one end of the concrete bar was fixed and the other end was free to move along the axial direction. A thermal expansion module was used in this study to account for the thermal expansion behavior of Fe-SMA during activation. Conductive heat transfer was defined between the SMA and concrete beam. Thermal insulation was applied to both ends of the SMA outside the concrete.

The geometrical model of the SMA strip (representing activation in air) is displayed in Fig. 1a; the concrete beam with an embedded SMA bar is displayed in Fig. 1b. A 3D solid structure model was used to represent the SMA and concrete beams during the modeling phase. Following the experimental setup used in previous studies [33,49,50], the SMA reinforcements were exposed to temperature change due to resistive electrical heating.

For developing the nonlinear material model for Fe-SMA, four main components were considered: elastic, thermal, plastic, and transformation strains. The elastic strain represents reversible deformations in material and is calculated based on Hook's law. The thermal strain components were calculated based on the material thermal expansion coefficient and the temperature change. Transformation strain is the key component of the SMA characteristics that correspond to the deformation of the martensite phase transformation in the material. For the Fe-SMA reinforcement, the plastic strain components were also added to the material model to capture the plastic behavior of Fe-SMA reinforcement during loading and unloading.

2.2. Constitutive material model

The simulation of Fe-SMAs differs significantly from that of Ni–Ti SMAs. The main difference in simulating Ni–Ti and Fe-SMAs lies in the constitutive models required to accurately capture their thermomechanical behaviors. Ni–Ti SMAs have well-established constitutive models, such as the Liang-Rogers and Souza-Auricchio models, which are widely recognized for their accuracy in simulating the SMA phase transformation, stress–strain relationships, and temperature-dependent behavior. These models allow for precise predictions of Ni–Ti SMAs' superelasticity and shape memory effect, which are relatively straightforward due to their stable, reversible transformation processes.

On the other hand, Fe-SMAs present additional complexities in simulation, primarily due to their different material properties, transformation characteristics, and significant plastic deformation. Unlike Ni–Ti, Fe-SMAs exhibit a mechanical behavior that involves a significant plastic deformation component, commonly attributed to stress- and temperature-induced transformations. This transformation presents an additional difference to Ni–Ti because Fe-SMAs do not exhibit fully reversible superelasticity at elevated temperatures. Furthermore, Fe-SMAs display a strain-hardening response, where transformation strain continues to increase with repeated thermal or stress cycles. Tailored models are therefore required to accurately simulate the transformation characteristics and mechanical responses of Fe-SMAs.

In the present study, the Lagoudas model [48,51] was used as the base for the calculation of the transformation strains in the multiphysical simulations. In Lagoudas' model, the Gibbs free energy density is a function of two state variables: the total stress tensor field (σ) and the temperature field (T). The transformation strain tensor field (ε_{tr}) and martensite volume fraction (ξ) are computed using additional internal variables. The compliance matrix (S) is established by averaging the elastic properties of martensite and austenite using volume averaging.

$$S(\xi) = \xi S_M + (1-\xi) S_A = S_A + \xi \Delta S, \tag{5}$$

where $\Delta S = S_M - S_A$. The other material parameters are similarly averaged. The evolution equation for the transformation strain ε_{tr} is derived from the flow rule as follows:

$$\dot{\varepsilon}_{tr} = \xi \Gamma, \tag{6}$$

where $\dot{\varepsilon}_{tr}$ is the time derivative of the transformation tensor. The variable representing the direction of the martensitic transformation ($\dot{\varepsilon}$), is computed from the previous state to determine the anticipated increase or decrease in ε_{tr}.

In the Lagoudas model, the phase transformation is described by six parameters: transformation temperatures M_s, M_f, A_s, and A_f, and the slopes of the austenite and martensite limit curves C_A and C_M, respectively. The relationships between the start and finish temperatures and stresses are as follows:

$$\sigma_{Ms} = C_M(T_\sigma - M_s)\ ,\ \sigma_{Mf} = C_M(T_\sigma - M_f)\ ,\ \sigma_{As} = C_A(T_\sigma - A_s)\ ,$$
$$\sigma_{Af} = C_A(T_\sigma - A_f), \tag{7}$$

where T_σ is the constant temperature at which the stress–strain curve was measured.

As the Lagoudas model is established for Ni–Ti type SMAs, the formulation should be modified to simulate the behavior of Fe-SMAs. In this regard, the nonlinear stress–strain behavior of the plastic component was incorporated to modify the Lagoudas model for Fe-SMA simulation. This enhancement provides a more accurate representation of the Fe-SMA behavior under loading conditions. The stress increment for the nonlinear plastic part is

$$\sigma = H\varepsilon^n, \tag{8}$$

where H and n are the strength coefficient and strain-hardening exponent, respectively.

For the Fe-SMA material, the phase diagram is displayed in Fig. 2. It includes two transformation zones for forward and reverse transformations. The diagram suggests that the formation of ε-martensite occurs primarily between the linear-elastic limit line and yield point of plastic deformation (shaded area in Fig. 2). The forward transformation zone is defined by the forward transformation starting line M_s and yielding line. At temperatures below the M_s line, both the γ- and ε-phases are stable, allowing the stress-induced ε-phase to persist even after unloading (i.e., martensite as the ε and austenite as the γ phase). The reverse transformation from the γ-phase to the ε-phase occurs at higher

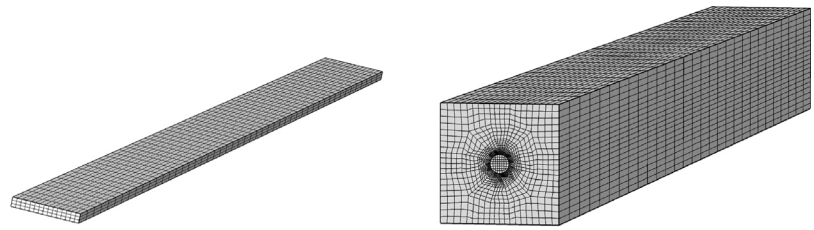

(a) (b)

Fig. 1. (a) Fe-SMA strip and (b) concrete bar with Fe-SMA bar.

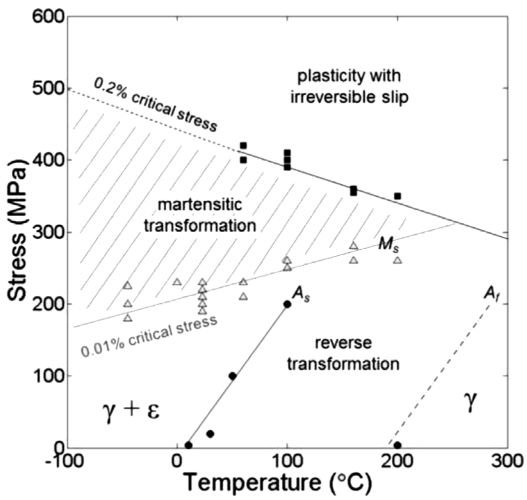

Fig. 2. Proposed diagram depicting the relationship between stress and temperature for Fe-SMA phase transformations [52].

Table 1
Material properties of Fe-SMA used in multiphysical simulation.

Property	Symbol	Value (unit)
Young's modulus (austenite)	E_A	160 (GPa)
Young's modulus (martensite)	E_M	90 (GPa)
Poisson's ratio	ν	0.3 (–)
Austenite start temperature	A_s	45 (°C)
Austenite finish temperature	A_f	190 (°C)
Martensite start temperature	M_s	−140 (°C)
Max. transformation strain	ε^L	4.1 (%)
Slope of martensite limit curve	C_M	2.1 (MPa/K)
Slope of austenite limit curve	C_A	3.4 (MPa/K)
Coefficient of thermal expansion	α	1.2 × 10^{-5} (1/K)
Thermal conductivity	κ	8.4 (W/m K)
Heat capacity	C_p	540 (J/kg K)
Electrical conductivity	Ω	0.5 × 10^6 (S/m)
Strain hardening exponent	n	16.86 (–)
Strength coefficient	H	926 (MPa)

temperatures between the A_s and A_f lines. When the temperature is above the A_f line, the ε phase is completely transformed into the γ phase. The A_s line for the reverse transformation zone is determined based on the 0.2% recovery strain points, whereas the A_f line is estimated from the recovery strain curve at 4 MPa, with both lines assumed to have the same slope in the phase diagram. Table 1 lists the material parameters of the Fe-SMA utilized in the multiphysical simulation. The modulus and transformation temperatures are obtained from experimental results on Fe-SMA. The plastic strain constants were obtained by curve fitting on the plastic strain, calculated by subtracting the transformation and elastic strains from the total strain component.

In the simulation, the Ottosen model criterion was used for the host concrete part. This model was developed for short-term concrete loads [53,54]. Table 2 lists the parameters selected for the concrete in the current study.

Table 2
Material properties of concrete used for multiphysical simulation.

Property	Symbol	Value (unit)
Young's modulus	E	23 (GPa)
Poisson's ratio	ν	0.2 (–)
Coefficient of thermal expansion	α	1.2 × 10^{-5} (1/K)
Uniaxial tensile strength	σ_t	20 (MPa)
Size factor	κ_1	11.8 (–)
Thermal conductivity	κ	1.3 (W/m K)
Heat capacity	C_p	1000 (J/kg K)
a	–	1.3 (–)
b	–	3.2 (–)
Shape factor	κ_2	0.98 (–)

3. Results and discussion

In the following sections, the findings of the experimental investigations were compared with the results of a multiphysical simulation, and the influence of geometrical and physical variables on the stress and deformation in reinforced concrete during activation was studied. The goal was to assess the accuracy and reliability of the multiphysical simulations.

3.1. Stress–strain behavior of Fe-SMA (Model I)

Using the input parameters for the SMA and modified formulation, the mechanical behavior of the SMA reinforcement was first investigated (Model I). The SMA bar was loaded statically, and its stress–strain behavior was obtained. Fig. 3 displays the contributions of the transformation, plastic, and elastic deformation phases to the stress–strain behavior of Fe-SMA. This breakdown enables a more in-depth examination of the SMA material response to loading. When the axial stress increases, the elastic portion of the SMA stress–strain curve is the first contributor to the axial strain. The second contribution is the transformation strain (ε_{tr}) which represents the phase transformation of the SMA beyond the elastic area. A stress-induced phase transformation was triggered in this region, resulting in the reorientation of martensitic variations. Ultimately, the SMA stress–strain curve reached the plastic strain. At this stage, the material developed persistent and irreversible deformation owing to dislocation motion and microstructural changes.

To validate the model, loading and unloading cycles on the Fe-SMA were considered. Fig. 4 displays the results of the previously published experimental investigation [33] and the current simulation for a loading-unloading cycle of a Fe-SMA specimen. Although the simulation predicted a marginally lower residual strain than the experiment, it aligned closely with the experimental results for both the loading and unloading stages. However, the model tends to overestimate the superelasticity effect. The discrepancy in recoverable strain arises from the interaction between plastic strain and transformation strain. Currently, a power law formulation is employed to calculate plastic strains. Utilizing a more advanced model, such as the Chaboche model, and

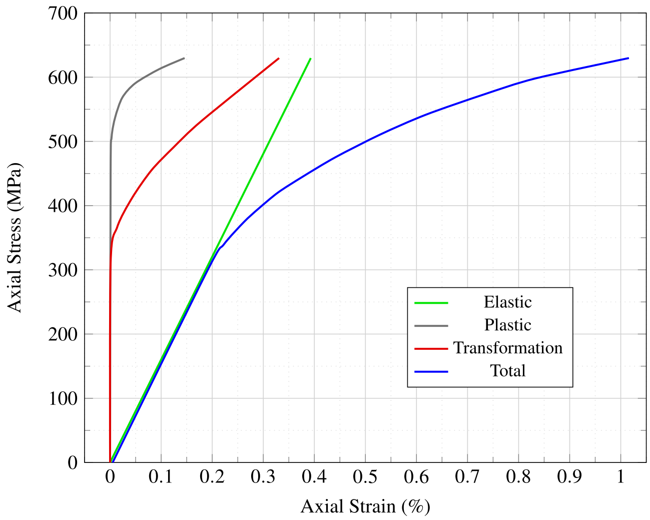

Fig. 3. Stress–strain curve for the SMA in tensile loading (total) and individual stress–strain components.

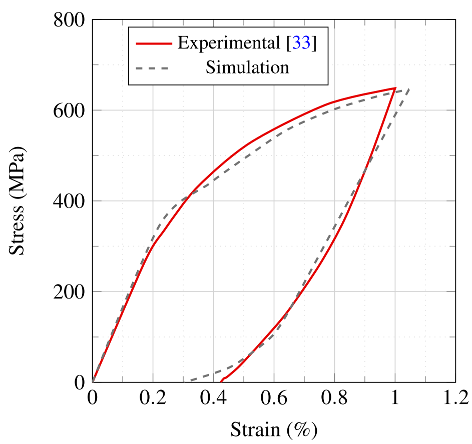

Fig. 4. Loading and unloading of Fe-SMA in experimental investigation and multiphysical simulation.

incorporating various stress levels to determine the model constants would improve unloading accuracy. Additionally, the lack of experimental data for material characterization introduces uncertainties in some input parameters related to transformation strains. Parameters such as the martensite finish temperature (M_f) and the transformation coefficient (C_a) significantly influence the transformation strain. The comparison of the results was also done for different strain levels. Fig. 5 displays the experimental investigation [33] and simulation results for the loading-unloading process of Fe-SMAs under different pre-straining conditions. The results of the multiphysical simulation align well with the experimental data. The obtained model for the Fe-SMA is used in the next steps for simulating the activation behavior in air and concrete.

3.2. Activation of fixed pre-strained Fe-SMA in air

In the experiments conducted by Shahverdi et al. [33] on the activation of Fe-SMA, a climate chamber was used in tensile testing to perform the heating during the test. This experiment using an air heating system was chosen as a verification step to eliminate the electric heating effect from the model. This approach allows focusing on the activation of the shape memory alloy through direct temperature application. The setup included a climatic chamber, clamps, a Fe-SMA test sample, and an extensometer (Fig. 6). The Fe-SMA strips were fixed at both ends and subjected to a pre-load of 30–40 MPa before the start of the heating tests to prevent compression within the test specimens during the heat-induced expansion. Subsequently, the temperature was gradually increased from 23 °C to 160 °C at a rate of 2 °C/min while the testing machine maintained a constant strain (i.e., no strain change). Following a 1–2 h delay at 160 °C, the temperature progressively decreased at a rate of approximately 2 °C/min until it reached 23 °C. The recovery stress values were determined by measuring the tensile stresses in the Fe-SMA strips after 1–2 h at 23 °C.

The stress–temperature relation of the 4% pre-strained Fe-SMA specimen in air is represented in Fig. 7, which compares the results of an experimental investigation and current multiphysical simulation. Within the temperature range of 20 °C to 40 °C, there was a distinct decline in stress for values less than 50 MPa. This decline is attributed to the thermal expansion effect experienced by the test specimens as the temperature increased. However, beyond 40 °C, the stress began to increase again. This increase in stress was attributed to the phase transformation from martensite to austenite. The stress reached a maximum of approximately 150 MPa at a maximum heating temperature of 160 °C. Subsequently, as the specimen cooled, the stress further increased owing to the thermal contraction effect. After a waiting period, the recovery stress was approximately 260 MPa. Fig. 8, displays the strain–temperature relationship in another experimental study [33], and the simulation results on activation of the same material. At an initial room temperature of 20 °C, during the activation, the temperature increased to 160 °C before gradually decreasing back to room temperature. The strain fluctuated considerably throughout this process, demonstrating an initial increase (tensile behavior) to approximately 0.03% below 50 °C, followed by a reduction to −0.37% (compressive behavior).

Based on the comparison of the results, the multiphysics model is able to simulate the activation behavior of the Fe-SMA in air. To validate the model in terms of heat transfer to concrete and stress transfer during activation, another experiment is also simulated in Section 3.3.

3.3. Activation of Fe-SMA reinforcement embedded in concrete

For a better examination of the model, two experimental studies were chosen for validation of the results of the activation of Fe-SMAs in concrete. Two different Fe-SMA geometries (strips and bars) were used in the experimental investigations.

3.3.1. Activation of flat Fe-SMA strip embedded in concrete

In experimental investigations by Czaderski et al. [49], ribbed Fe-SMA strips with a nominal thickness of 1.6 mm were centrally embedded in concrete bars (Fig. 9). Three thermocouples were attached to the Fe-SMA strips before casting the concrete to monitor the temperature on the surfaces of the strips inside the concrete bars. The Fe-SMA strips were triggered by resistive heating after the concrete was cured to induce compressive stress. A current density of approximately 14 A/mm^2 was used to rapidly obtain a concrete strip temperature of 150 °C. The power supply was cut off after the temperature was reached. Despite disabling the power source, the temperature continued to increase and eventually reached 160 °C throughout the experiment.

The obtained results of the multiphysical simulation for the Fe-SMA strip embedded in concrete were presented and compared with those obtained by Czaderski et al.'s [49] experimental investigation. Fig. 10 displays the temperature–time relationship of the Fe-SMA strip embedded in concrete throughout the experiment (T1 temperature in [49]), and multiphysical simulation. Considering a room temperature of 20 °C in both approaches, the temperature was increased by the start of the activation process to 160 °C after approximately 7 s and decreased to 110 °C after 15 s. The results demonstrated good agreement between the experimental investigations and multiphysical simulations.

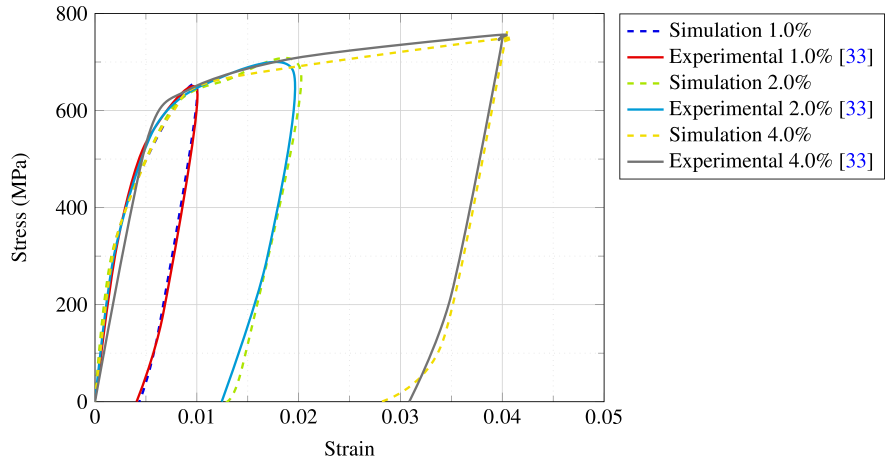

Fig. 5. Stress–strain relationship of Fe-SMA with different pre-strain levels based on experimental testing and multiphysical simulation.

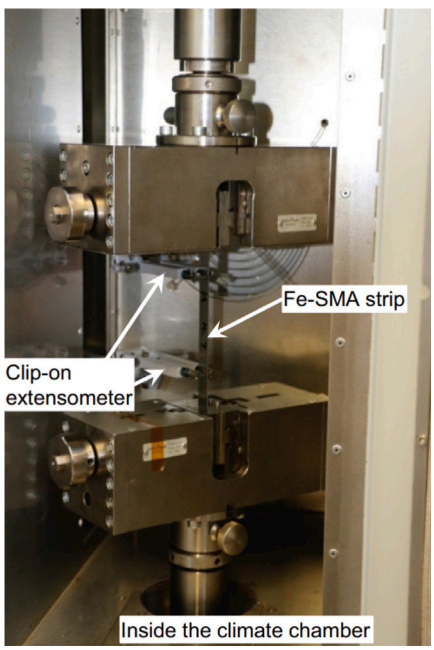

Fig. 6. 20 kN Zwick machine equipped with climate-controlled chamber used for pre-straining and activation of Fe-SMA test specimens [33].

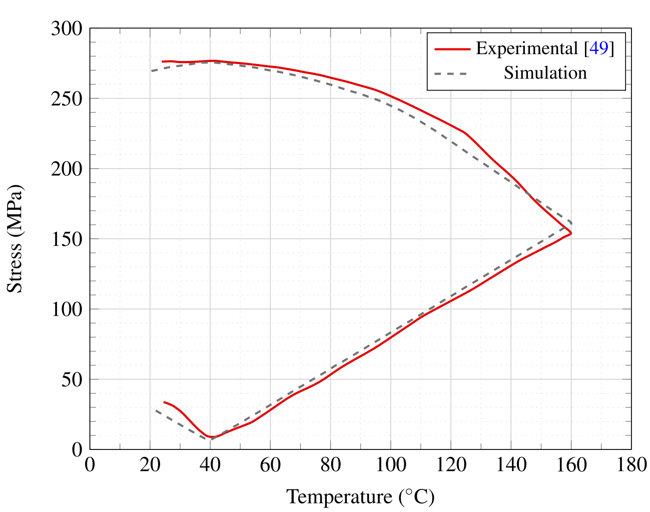

Fig. 7. Stress–temperature relationship of Fe-SMA for 4.0% pre-strain level.

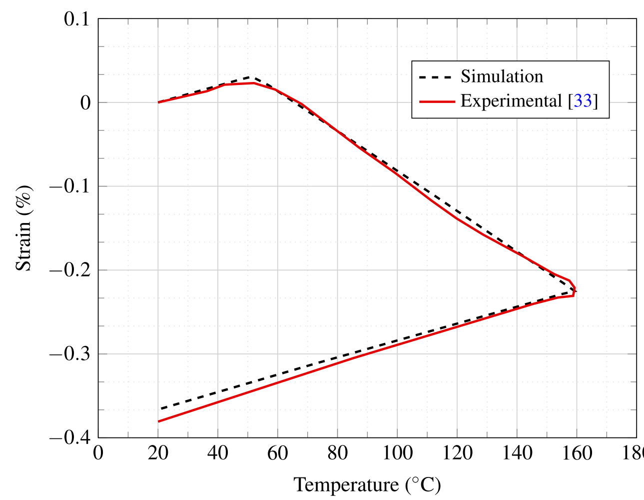

Fig. 8. Strain–temperature relationship of Fe-SMA for 4.0% pre-strain level.

The temperature distribution over the cross section at three distinct time steps of the multiphysical simulation is displayed in Fig. 11. At t = 0 s, Fe-SMA and concrete had the same temperature as the room temperature of 20 °C. At t = 10 s, the core temperature of the Fe-SMA strip reached 160 °C; the surrounding concrete absorbed part of this thermal energy because of its thermal conductivity. More thermal energy was transmitted from the Fe-SMA strip to the concrete after 30 s of activation, resulting in temperatures ranging from 40 °C to 65 °C for both materials. Fig. 12a displays the temperature distribution 15 s after the start of the activation process. The temperature transfer from Fe-SMA to all corners of the concrete matrix can be observed in the cross-section. As indicated in Fig. 12b, after approximately 60 s of activation, the temperature difference between the concrete and Fe-SMA strip was less than 3 °C, demonstrating the thermally stable behavior of the concrete and Fe-SMA material after activation.

Fig. 13 displays the temperature fluctuation at the midline of the beam cross-section at different intervals throughout the activation process. A uniform temperature distribution was observed at t = 0 s, which was equal to the room temperature of 20 °C. The core temperature of the cross-section (middle of the Fe-SMA section) exceeded 200 °C after applying the activation temperature to the Fe-SMA strip for t = 3 s. After 60 s, the temperature in the cross-sectional midline remained at approximately 50 °C. Fig. 14 displays the displacement of the beam at different times during the activation process. The beam expanded marginally by 0.015 mm after 2 s and then contracted to 0.07 mm after

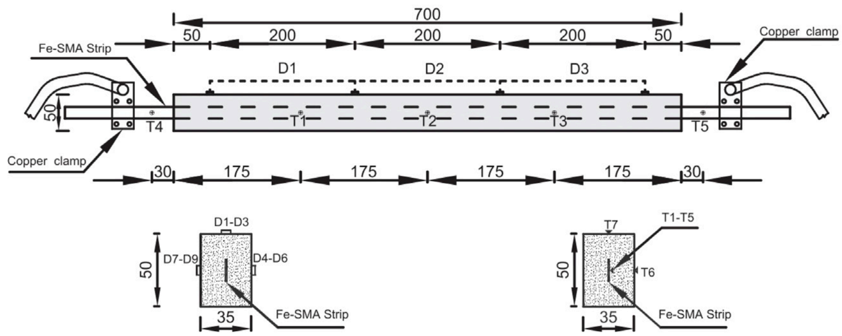

(a)

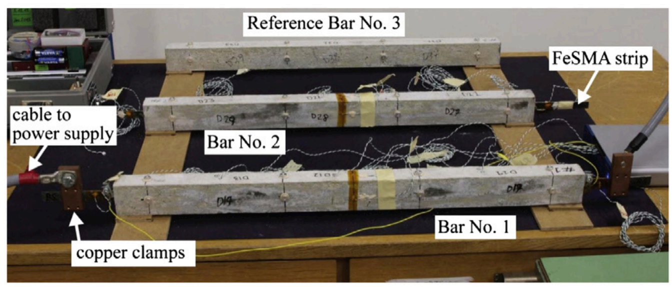

(b)

Fig. 9. Experimental investigation of embedded Fe-SMA strip in concrete bar: (a) concrete bar size, as well as positioning of mechanical strain gauges and temperature measurement locations (units in mm) and (b) experiment set up [49].

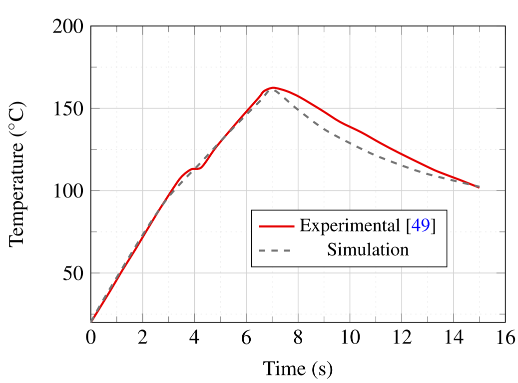

Fig. 10. Temperature of Fe-SMA strip embedded in concrete during experimental investigation and multiphysical simulation.

90 s. This contraction of the beam could enhance the stiffness of the concrete material, which supports the idea of using Fe-SMA materials for pre-stressing concrete structures. The initial thermal expansion of the concrete and Fe-SMA strip before the temperature exceeded the martensitic phase transformation starting point could explain the occurrence of an overall expansion at this stage. The concrete and Fe-SMA expand owing to thermal expansion and subsequently contract owing to the shape-memory effect.

Fig. 15a displays the first stage of expansion, followed by contraction over a long period. Starting at 500 s, the value reflecting the decrease in placement remained comparatively stable at approximately 0.07 mm, with only minor fluctuations up to 3000 s. Furthermore, it is evident from Fig. 15b that early tensile stresses of approximately 0.5 MPa developed when the stress values in the concrete beam were examined. Subsequently, the compressive stress in the beam increased to 3.5 MPa in 500 s and remained steady for the next 2500 s.

3.3.2. Activation of rounded Fe-SMA bar embedded in concrete

Another set of experiments [50] involved embedding ribbed Fe-SMA bars with a nominal diameter of 8 mm into concrete specimens with dimensions of 700 mm × 50 mm × 50 mm. The temperature during the activation was measured using thermocouples positioned on the bar surface. Following the casting of the concrete, two additional thermocouples were installed on the surface of the rod and two on the surface of the concrete. Fig. 16 displays the experimental layout. The first electric impulse was set to 6 v to coordinate the electrical potential. Despite this modest potential, only a minor increase in the temperature was observed. Another potential of 8.6 v was applied after further alignment and cooling to ambient temperature. An electric current was employed in both the activation techniques for the Fe-SMA bar and strip to initiate the phase transformation in the Fe-SMA via electrical conductivity. The distinction is that, in the case of the Fe-SMA strip, a capacitor configuration was employed for activation.

The temperature–time evolution of the Fe-SMA bars embedded in concrete is shown in Fig. 17, which includes the experimental (averaged data) and multiphysical results. Assuming a starting room temperature of 20 °C under all circumstances, the temperature increased to approximately 150 °C after 5 s of activation and then continuously declined, reaching 30 °C after 1200 s. The results demonstrated good agreement between the experimental investigations and multiphysical simulations.

As presented in the experimental study [50], the insulating tape introduced a temporal delay in the peak in Fig. 18. The time required for heat to diffuse through the thin tape accounts for this delay. Furthermore, creating a faultless connection between the tape and thermocouples was difficult because of the uneven surface of the rod, which is purposefully damaged to improve its adhesion with the concrete. Fig. 18a displays the temperature distribution over the cross-section at

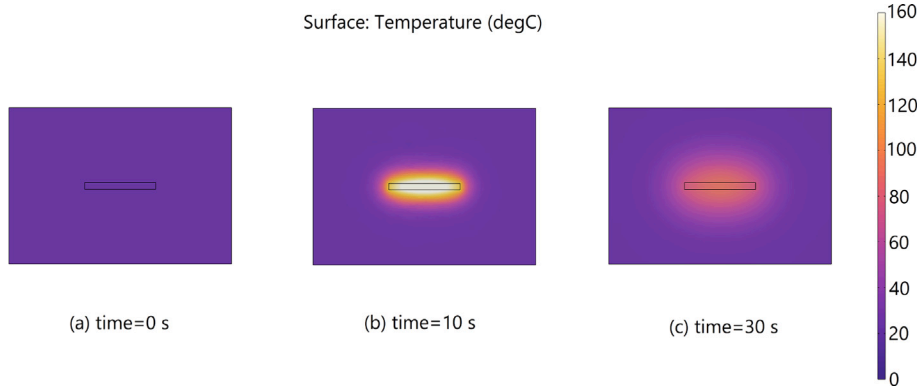

Fig. 11. Temperature distribution in cross section at different times in multiphysical simulation.

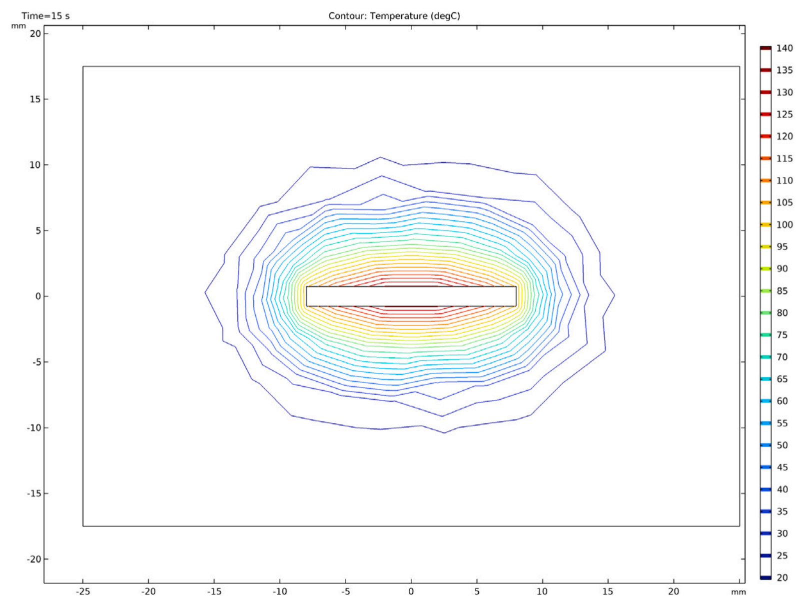

(a) t = 15 s

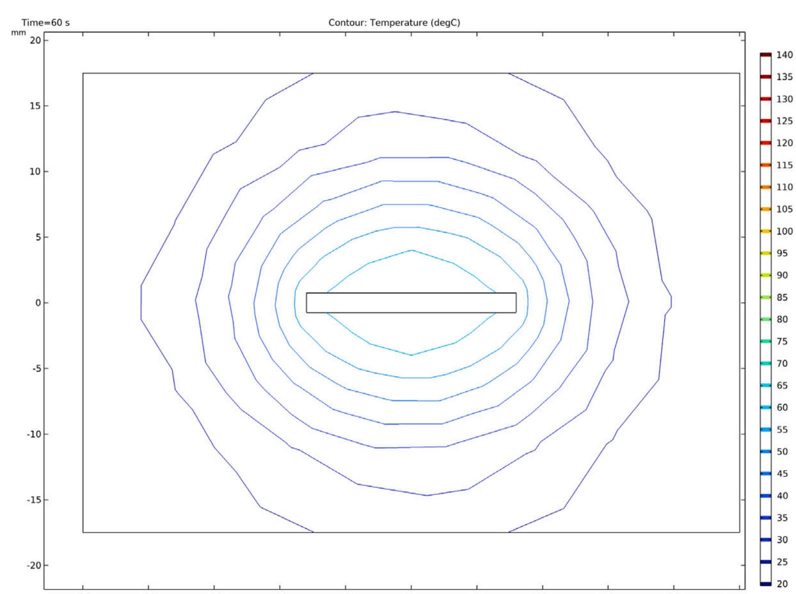

(b) t = 60 s

Fig. 12. Temperature distribution of cross-section in multiphysical simulation: (a) at time = 15 s and (b) at time = 60 s.

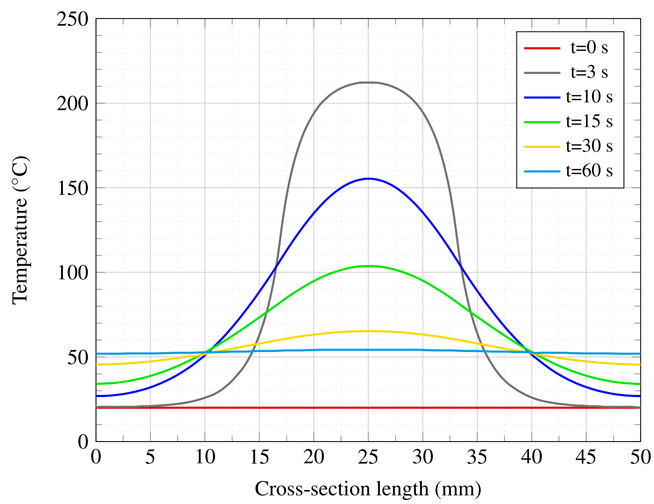

Fig. 13. Variation of temperature in midline of cross-section.

t = 15 s. The temperature distribution was similarly uniform owing to the symmetrical geometry of the concrete and Fe-SMA bar. As indicated in Fig. 18b, after approximately 60 s of activation, the temperature difference between the concrete and Fe-SMA bar was approximately 19 °C. By comparing the temperature–time diagrams for the Fe-SMA bar and strip, it is noticeable that the temperature decrease in the Fe-SMA bar was more gradual than that in the Fe-SMA strip. This difference could be attributed to the Fe-SMA bar sample having a larger surface area (approximately 27.0%) and a higher volume percentage of Fe-SMA in the concrete (approximately 25.0%) than the Fe-SMA strip sample. Section 3.4 presents a comparison of the Fe-SMA bar and strip activation.

A comparative analysis of the simulated and experimental displacements of the concrete beam during the first 60 s of activation is presented in Fig. 19. Although the experimental setup encompassed the recording of different displacements along the four edges of the beam, the simulated outcomes indicated uniform displacements across all edges. In the absence of an explanation for the variations in the edge displacements in [50], a potential reason could be the marginal eccentricity of the SMA bar embedded in the concrete beam.

For clarity, a supplementary simulation was conducted by introducing eccentricity into the SMA. To achieve this, the SMA bar was intentionally offset by 2 mm in both vertical and horizontal orientations. The displacement results for the beam simulation that incorporated this eccentricity are displayed in Fig. 20. Fig. 20 displays a significant difference in the displacement values across the distinct edges following the introduction of even minor eccentricity. This supports the hypothesis of initial eccentricity within the experimental specimen. Notably, the effect of self-weight on the difference in displacement at the edges was calculated to be negligible. Owing to the thermal expansion of the Fe-SMA bar, the average stress in the concrete began to increase (tensile) from the beginning of the activation phase. As indicated in Fig. 21, the phase transformation in the Fe-SMA bar occurred after approximately 5 s, and the bars transmitted pressure to the concrete section, thereby reducing the stresses (compressive). The measured compressive stress increased after activation.

Fig. 22, displays a displacement–time plot of the Fe-SMA bar after activation for 600 s. The simulation continued for 600 s to obtain a complete stress cycle for the Fe-SMA. Following an initial decrease in displacement until the 60-s point (due to an increase in concrete temperature and subsequent expansion of the concrete bar), there was an increase in displacement from 60 s to 200 s. This increase occurred when the concrete temperature decreased, removing the thermal expansion effect and allowing the SMA to exert compressive stresses. The stress values of the Fe-SMA bar embedded in the concrete during the activation process are displayed in Fig. 23. The results indicate that at the start of the activation process, for the temperature ranges of room temperature (20 °C) and 55 °C, stress levels below 50 MPa decreased, indicating that tensile stress was generated by thermal expansion. Consequently, as the temperature increased, the stress levels also increased, peaking at a given temperature point. Following this peak, a marginal decrease in the temperature caused a continual increase in the stress levels, reaching approximately 220 MPa. This value is marginally lower than the recovery stress previously indicated in Fig. 7, in which the sample was fixed at both ends. However, there was displacement in the beam in the present situation.

3.4. Parametric study of Fe-SMA activation in concrete

Following the verification of the multiphysics model in multiple steps, a parametric analysis of the effective physical and geometrical parameters such as the volume fraction and pre-strain level of Fe-SMA elements is presented in this section. It is essential to note that the activation procedure and the dimensions of concrete beams utilized in this section are identical to those used in the experiments previously discussed for all scenarios. First, the effect of the size (volume fraction) of the SMA reinforcement is studied. In this regard, the impact of increasing the Fe-SMA diameter from 2 to 10 mm at 2 mm intervals on the temperature throughout the activation phase is displayed in Fig. 24. The temperature progressively decreased over time; a smaller diameter attained a steady temperature more quickly than a larger diameter. A specimen with a diameter of 2 mm reached ambient temperature in approximately 150 s; a sample with a diameter of 10 mm required more than 1000 s to reach a steady level of approximately 50 °C. Fig. 25, displays the effect of changing the Fe-SMA diameter from 2 to 10 mm in 2 mm increments on the beam displacement. The average displacement initially increased with the nominal diameter increase of the Fe-SMA. However, after approximately 4 s, the difference became significant. The Fe-SMA with a diameter of 10 mm exhibited the greatest displacement (0.08 mm), whereas the one with a diameter of 2 mm exhibited negligible changes over the 15 s activation period. Consequently, it can be assumed that increasing the diameter of the Fe-SMA by 2 mm increases the ultimate displacement (and compressive stress) by 40%–60%.

In addition to the diameter of the Fe-SMA bar, another effective parameter is the pre-strain level in the Fe-SMA. Fig. 26, displays the effect of different pre-straining levels (0, 1.0, 2.0, and 4.0%) on the displacement of the beam. Due to the absence of phase transformation and lack of the shape-recovery effect, a component without any pre-straining behaves similarly to conventional metallic materials. Conversely, pre-strained Fe-SMA materials lead to different behaviors, with larger pre-strain levels resulting in larger displacement in the specimens. The effect of the recovery stress is similar for Fe-SMA pre-straining levels of 2.0% and 4.0%. This result is consistent with the experimental results reported by Shahverdi et al. [33]. Consequently, employing a 2.0% pre-straining level could be the optimal choice because it provides the same effects requiring less work during the pre-straining stage. Fig. 27, displays the impacts of different pre-straining levels (with values identical to those in Fig. 26) for the stress level in concrete. As there is no phase transformation in Fe-SMA with no pre-strain level, only the effect of thermal expansion and consequent tensile stresses are obtained in this species. However, in the pre-strained samples, a pattern similar to that in the preceding figure (Fig. 26) occurs, where increasing the pre-straining level leads to higher levels of induced compressive stresses (pre-stressing level). It is noteworthy that when the tensile strength of concrete and its susceptibility to cracking due to tensile stresses are considered, the level of pre-strain becomes relevant. Compared to the pre-strain values demonstrated

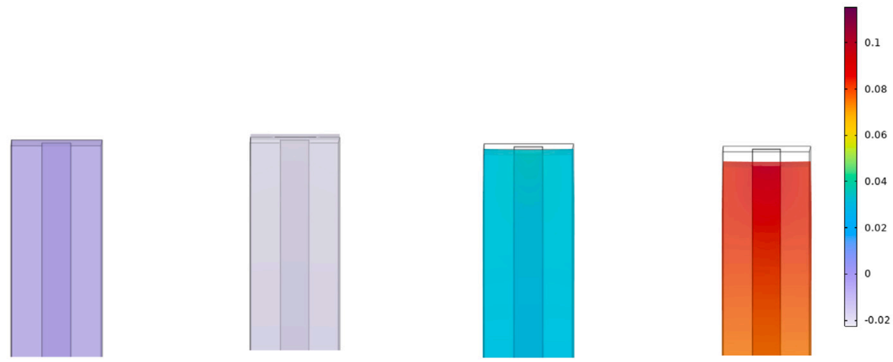

(a) Initial state

(b) Thermal expansion of Fe-SMA

(c) Applied compressive recovery force from Fe-SMA

(d) Maximum compressive deformation of beam

Fig. 14. Displacement of the beam at different times following activation process (units: mm).

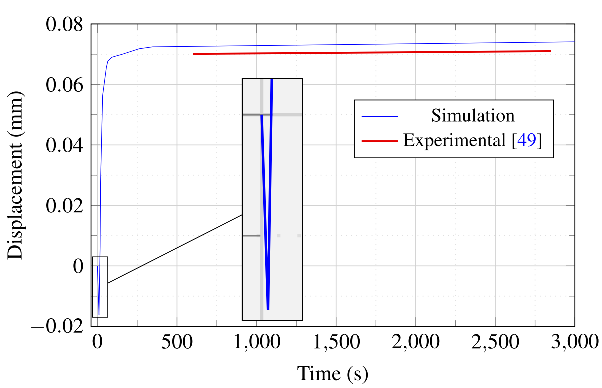

(a)

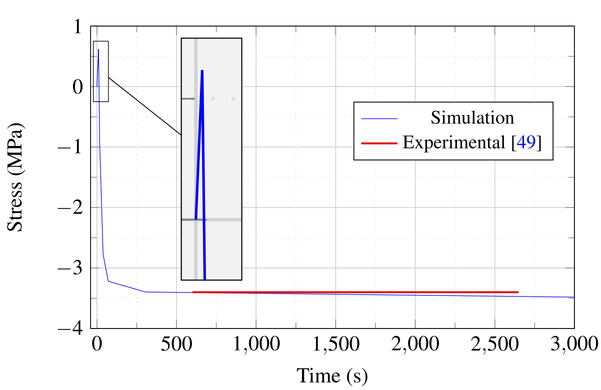

(b)

Fig. 15. Time-dependent variation of (a) displacement and (b) stress in concrete beam.

in this study, the corresponding tensile strains remained below the crucial cracking threshold. However, it is vital to note that the 0% pre-strained specimen could experience cracking and subsequent damage to the concrete. Fig. 28, displays the effect of changing the Fe-SMA strip thickness from 10 to 15, 20, 30, and 40 mm on the temperature during the 60 s stimulation procedure. As the strip thickness increased, all samples exhibited a similar temperature increase (slope) of up to 160 °C over the first 8 s. However, the temperature began to decrease beyond this point, with marginally distinct slopes for each specimen. The specimen with a thickness of 10 mm exhibited the sharpest temperature reduction, whereas the thickest sample (40 mm) exhibited the smallest temperature decrease. Fig. 29, displays the effect of altering the Fe-SMA strip width from 10 to 15, 20, 30, and 40 mm on the edge displacement during the 3000-s activation procedure. As the strip thickness increased, a constant and continuous increase in displacement was observed, indicating a clear and direct link between the Fe-SMA strip width and displacement experienced in the specimen.

Another target of the parametric study was to compare the temperature distributions and variations between the two types of reinforced specimens. One specimen included a Fe-SMA strip; the other included a Fe-SMA bar. This comparison was performed under specified simulation conditions:

- Both beams had the same specimen cross-section, which matched the Fe-SMA strip tests conducted by Czaderski et al. [49].
- A comparable electric activation on both samples was used, following the methods used by Czaderski et al. [49].
- The cross-sectional areas of the bar and strip were identical, ensuring that the volume fraction of Fe-SMA remained consistent throughout the two scenarios. The main difference was in the contact area between the bar and strip, which was directly connected to the basic characteristics of the SMA perimeters.

The temperature profile 60 s after activation in both cases, Fe-SMA strip and bar is shown in Fig. 30. It can be observed that both cases attained their peak temperatures of 270 °C and 155 °C, respectively, virtually within 6 s. The temperature decreased after the maximum point in both cases, and after 60 s the Fe-SMA bar remained 17 °C warmer than the strip. The temperature patterns of both specimens after 10 s are displayed in Fig. 31. The peak temperature was considerably higher for the Fe-SMA bar, demonstrating a variation in the temperature distribution due to the use of different Fe-SMA shapes.

4. Conclusions

The key findings of this study are as follows.

- The presented multiphysics model, which is based on the modified Laogudas constitutive model for SMA, can simulate the stress–strain behavior of Fe-SMA during free and forced activations.

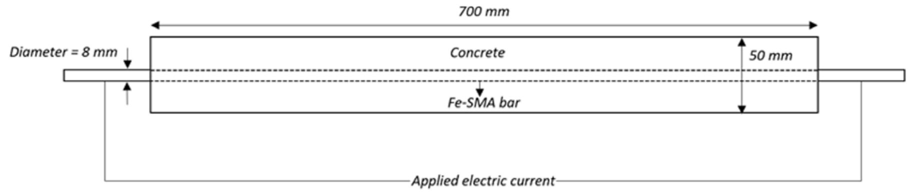

(a)

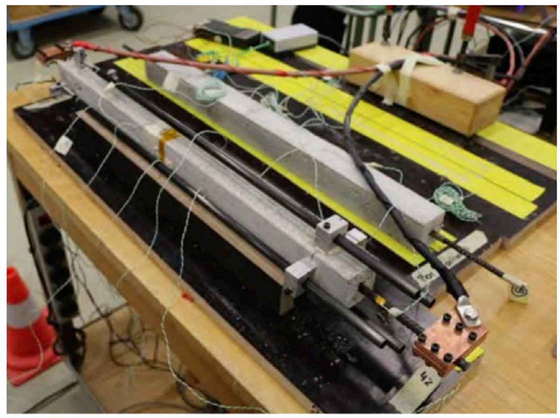

(b)

Fig. 16. Schematic of the experimental setup of rounded Fe-SMA reinforcement in concrete used in [50].

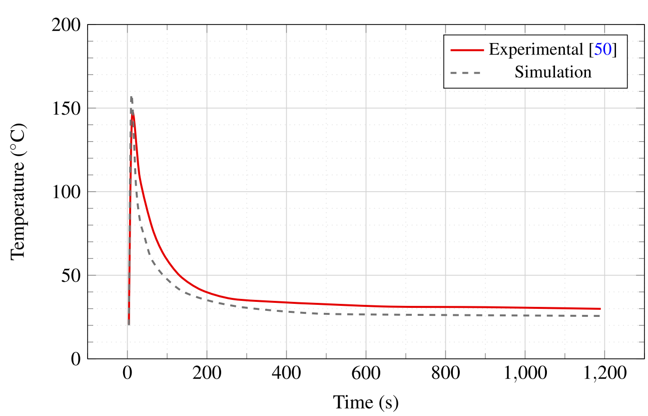

Fig. 17. Temperature of rounded Fe-SMA reinforcement during experimental investigation and multiphysical simulation.

- The activation of Fe-SMA inside the concrete bar was simulated and aligned well with the experimental results. Two different states of initial tension followed by subsequent compression were displayed in the concrete bar upon activation of the embedded SMA.
- The degree of pre-strain in Fe-SMA has a significant influence on its thermodynamic behavior. Conversely, when the pre-strain level was increased from 1.0% to 4.0%, the negative stresses in the concrete (i.e., compressive stresses resulting in a pre-stressing effect) also increased. Based on the findings of this research, a 2% pre-straining level can be regarded as the ideal strain level for activation.
- When comparing the findings of specimens with Fe-SMA bars and strips, it was discovered that the temperature distribution in the specimen with Fe-SMA bars is more uniform because it has a symmetrical cross-section. Furthermore, the temperature reduction was faster in the sample with the Fe-SMA bar because it shared a larger surface area with the concrete matrix.

CRediT authorship contribution statement

Ali Saeedi: Writing – original draft, Software, Methodology, Investigation, Conceptualization. **Alireza Tabrizikahou:** Writing – review & editing, Writing – original draft, Software, Investigation. **Paul-Remo Wagner:** Writing – review & editing, Methodology, Investigation. **Moslem Shahverdi:** Writing – review & editing, Supervision, Project administration, Conceptualization.

Declaration of competing interest

The authors declare that they have no known competing financial interests or personal relationships that could have appeared to influence the work reported in this paper.

Data availability

Data will be made available on request.

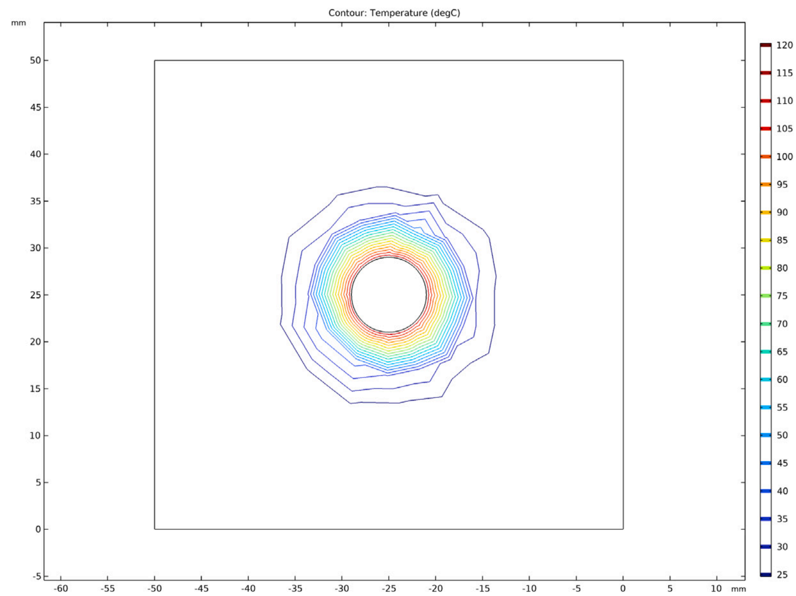

(a) t = 15 s

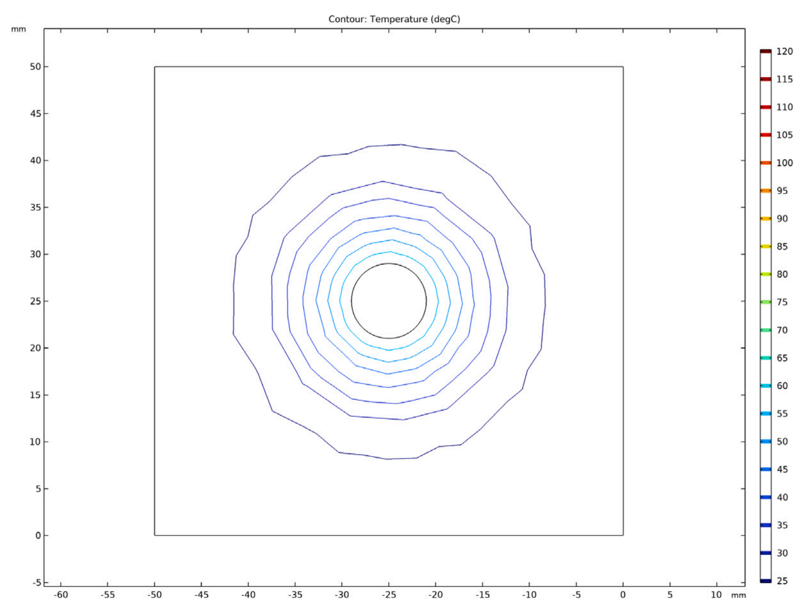

(b) t = 60 s

Fig. 18. Temperature distribution pattern of cross-section at t = 60 s in the multiphysical simulation: (a) at t = 15 s and (b) at t = 60 s.

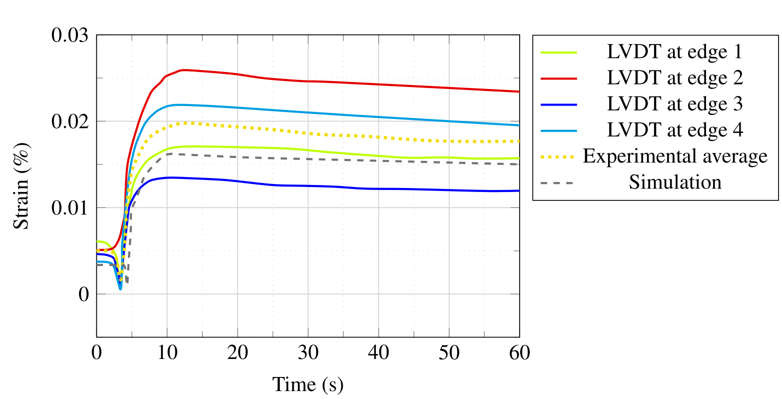

Fig. 19. Axial strain in concrete beam during experimental investigations and multiphysical simulation.

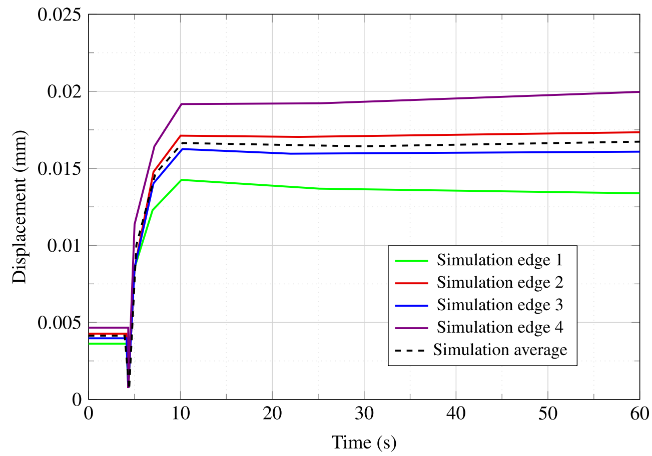

Fig. 20. Displacement in concrete beam during experimental investigations and multiphysical simulation.

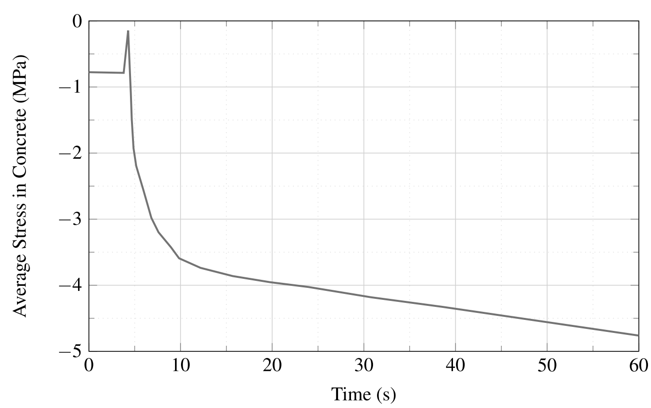

Fig. 21. Variation of stress in concrete during analysis.

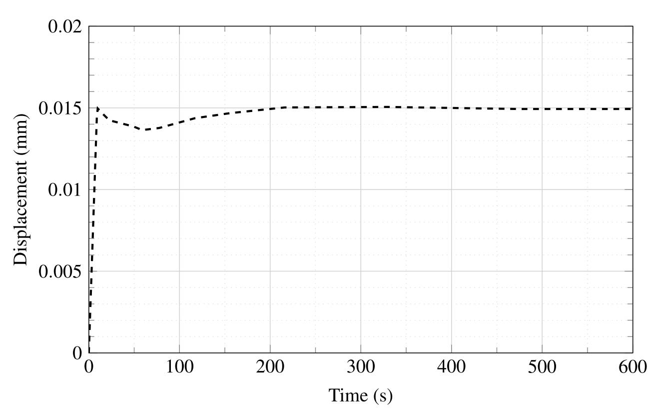

Fig. 22. Variation of displacement in the sample during analysis.

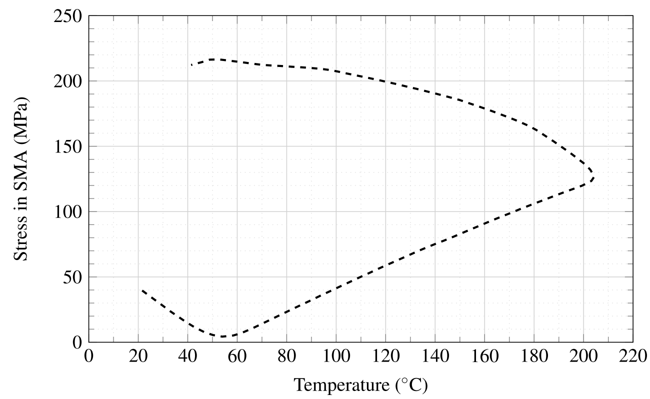

Fig. 23. Stress–temperature curves for Fe-SMA reinforcement during analysis.

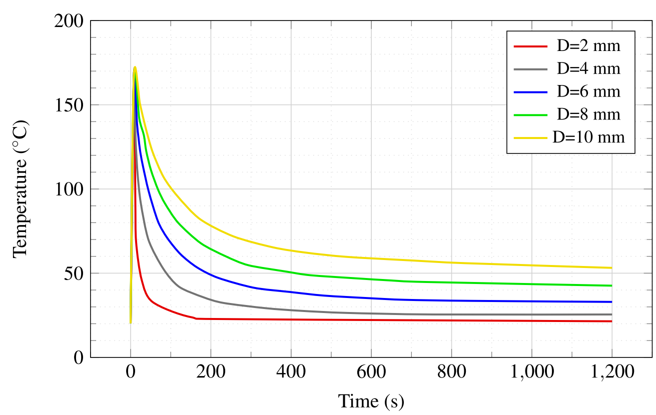

Fig. 24. Effect of Fe-SMA bar diameter on temperature variation.

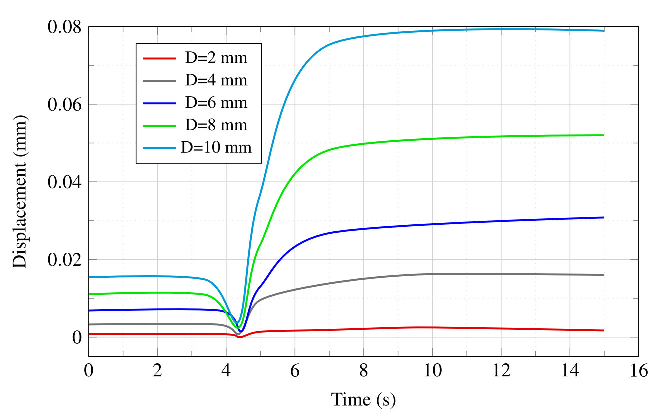

Fig. 25. Effect of Fe-SMA bar diameter on displacement variation.

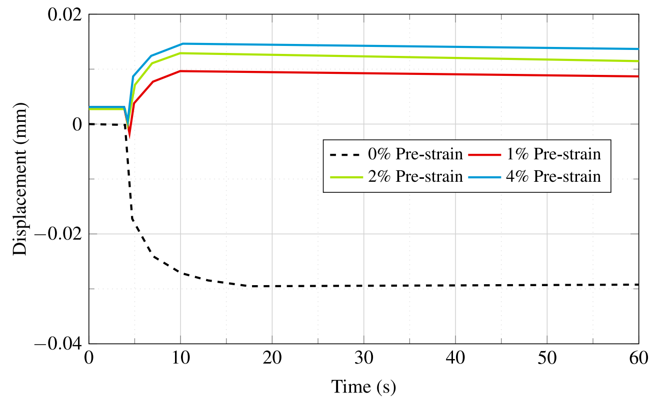

Fig. 26. Effect of pre-strain level in Fe-SMA bar on displacement during activation.

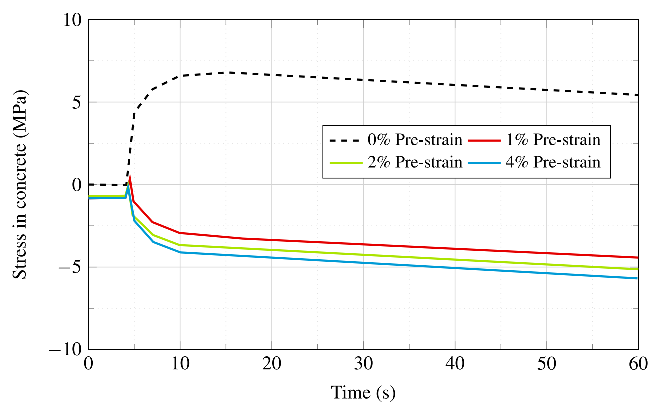

Fig. 27. Effect of pre-strain level in Fe-SMA bar on stress values in concrete during activation.

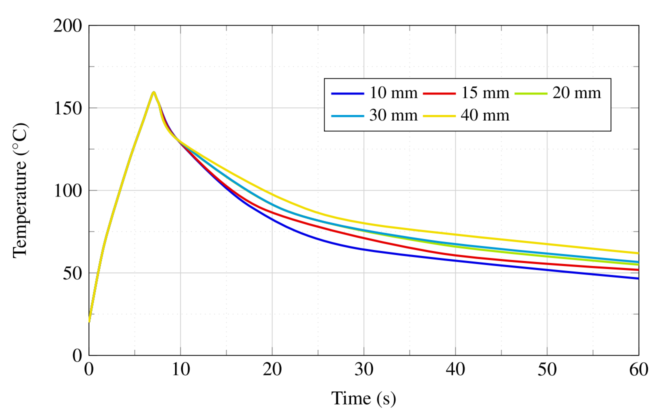

Fig. 28. Effect of Fe-SMA strip thickness on temperature variation during activation.

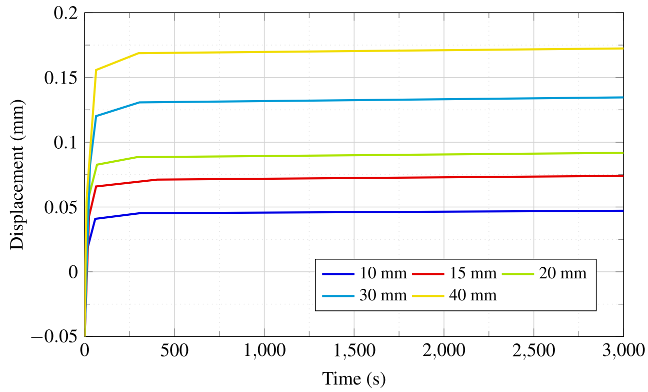

Fig. 29. Effect of Fe-SMA strip thickness on displacement variation during activation.

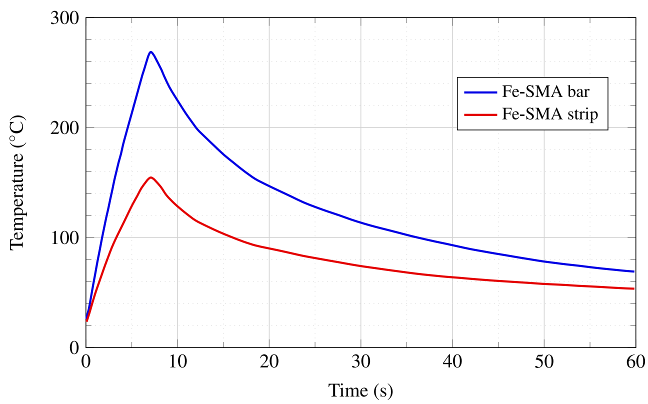

Fig. 30. Temperature–time relationship of both samples 60 s after activation.

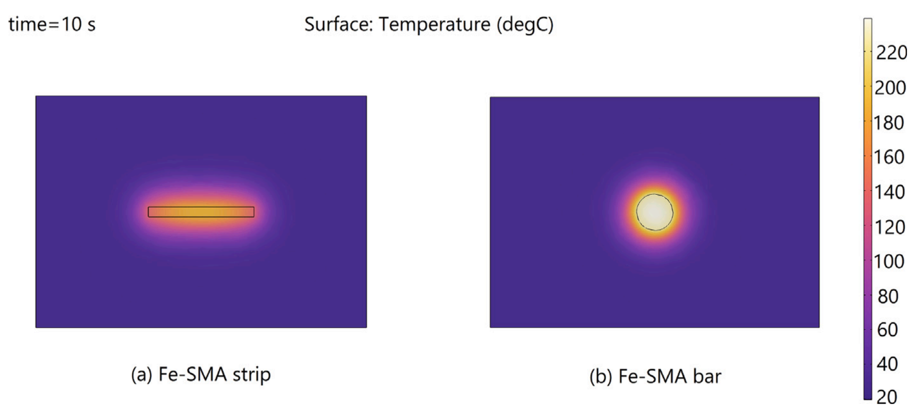

Fig. 31. Temperature distribution in samples with Fe-SMA strip and bar after 10 s of activation.

References

[1] Tabrizikahou A, Kuczma M, Nowotarski P, Kwiatek M, Javanmardi A. Sustainability of civil structures through the application of smart materials: A review. Materials 2021;14(17):4824. http://dx.doi.org/10.3390/ma14174824.

[2] Zareie S, Issa AS, Seethaler RJ, Zabihollah A. Recent advances in the applications of shape memory alloys in civil infrastructures: A review. Structures 2020;27:1535–50. http://dx.doi.org/10.1016/j.istruc.2020.05.058.

[3] Tabrizikahou A, Kuczma M, Łasecka-Plura M, Noroozinejad Farsangi E, Noori M, Gardoni P, Li S. Application and modelling of Shape-Memory Alloys for structural vibration control: State-of-the-art review. Constr Build Mater 2022;342:127975. http://dx.doi.org/10.1016/j.conbuildmat.2022.127975.

[4] Mas B, Biggs D, Vieito I, Cladera A, Shaw J, Martínez-Abella F. Superelastic shape memory alloy cables for reinforced concrete applications. Constr Build Mater 2017;148:307–20. http://dx.doi.org/10.1016/j.conbuildmat.2017.05.041.

[5] Mohd Jani J, Leary M, Subic A, Gibson MA. A review of shape memory alloy research, applications and opportunities. Mater Des (1980-2015) 2014;56:1078–113. http://dx.doi.org/10.1016/j.matdes.2013.11.084.

[6] Janke L, Czaderski C, Motavalli M, Ruth J. Applications of shape memory alloys in civil engineering structures—Overview, limits and new ideas. Mater Struct 2005;38(5):578–92. http://dx.doi.org/10.1007/BF02479550.

[7] Fang C. SMAs for infrastructures in seismic zones: A critical review of latest trends and future needs. J Build Eng 2022;57:104918. http://dx.doi.org/10.1016/j.jobe.2022.104918.

[8] Fang C, Ping Y, Zheng Y, Chen Y. Probabilistic economic seismic loss estimation of steel braced frames incorporating emerging self-centering technologies. Eng Struct 2021;241:112486. http://dx.doi.org/10.1016/j.engstruct.2021.112486.

[9] Fang C, Yam MC. Emerging superelastic SMA core damping elements for seismic application. Front Built Environ 2023;8. http://dx.doi.org/10.3389/fbuil.2022.953273.

[10] Fang C, Yam MC, Lam AC, Xie L. Cyclic performance of extended end-plate connections equipped with shape memory alloy bolts. J Constr Steel Res 2014;94:122–36. http://dx.doi.org/10.1016/j.jcsr.2013.11.008.

[11] Yam MC, Fang C, Lam AC, Zhang Y. Numerical study and practical design of beam-to-column connections with shape memory alloys. J Constr Steel Res 2015;104:177–92. http://dx.doi.org/10.1016/j.jcsr.2014.10.017.

[12] Debska A, Gwozdziewicz P, Seruga A, Balandraud X, Destrebecq JF. Prestress state evolution during thermal activation of memory effect in concrete beams strengthened with external SMA wires. Arch Civ Mech Eng 2020;20(4):142. http://dx.doi.org/10.1007/s43452-020-00133-y.

[13] Tabrizikahou A, Białasik J, Borysiak S, Fabisiak M, Łasecka M. Shear strengthening of damaged reinforced concrete beams with iron - based shape memory alloy (fe - SMA) strips : numerical and parametric analysis. Arch Civ Mech Eng 2024;6. http://dx.doi.org/10.1007/s43452-024-01004-6.

[14] Raza S, Michels J, Shahverdi M. Uniaxial behavior of pre-stressed iron-based shape memory alloy rebars under cyclic loading reversals. Constr Build Mater 2022;326:126900. http://dx.doi.org/10.1016/j.conbuildmat.2022.126900.

[15] Ghafoori E, Neuenschwander M, Shahverdi M, Czaderski C, Fontana M. Elevated temperature behavior of an iron-based shape memory alloy used for prestressed strengthening of civil structures. Constr Build Mater 2019;211:437–52. http://dx.doi.org/10.1016/j.conbuildmat.2019.03.098.

[16] Moser K, Bergamini A, Christen R, Czaderski C. Feasibility of concrete prestressed by shape memory alloy short fibers. Mater Struct 2005;38(5):593–600. http://dx.doi.org/10.1007/BF02479551.

[17] Schranz B, Nunes MF, Czaderski C, Shahverdi M. Fibre optic strain measurements for bond modelling of prestressed near-surface-mounted iron-based shape memory alloy bars. Constr Build Mater 2021;288:123102. http://dx.doi.org/10.1016/j.conbuildmat.2021.123102.

[18] Schranz B, Michels J, Czaderski C, Motavalli M, Vogel T, Shahverdi M. Strengthening and prestressing of bridge decks with ribbed iron-based shape memory alloy bars. Eng Struct 2021;241:112467. http://dx.doi.org/10.1016/j.engstruct.2021.112467.

[19] Tabrizikahou A, Kuczma M, Łasecka-Plura M. Out-of-plane behavior of masonry prisms retrofitted with shape memory alloy stripes: Numerical and parametric analysis. Sensors 2022;22(20):8004. http://dx.doi.org/10.3390/s22208004.

[20] Tabrizikahou A, Kuczma M, Łasecka-Plura M, Noroozinejad Farsangi E. Cyclic behavior of masonry shear walls retrofitted with engineered cementitious composite and pseudoelastic shape memory alloy. Sensors 2022;22(2):511. http://dx.doi.org/10.3390/s22020511.

[21] Tabrizikahou A, Hadzima-Nyarko M, Kuczma M, Lozančić S. Application of shape memory alloys in retrofitting of masonry and heritage structures based on their vulnerability revealed in the bam 2003 earthquake. Materials 2021;14(16):4480. http://dx.doi.org/10.3390/ma14164480.

[22] Raza S, Widmann R, Michels J, Saiid Saiidi M, Motavalli M, Shahverdi M. Self-centering technique for existing concrete bridge columns using prestressed iron-based shape memory alloy reinforcement. Eng Struct 2023;294:116799. http://dx.doi.org/10.1016/j.engstruct.2023.116799.

[23] Raza S, Shafei B, Saiid Saiidi M, Motavalli M, Shahverdi M. Shape memory alloy reinforcement for strengthening and self-centering of concrete structures—State of the art. Constr Build Mater 2022;324:126628. http://dx.doi.org/10.1016/j.conbuildmat.2022.126628.

[24] El-Hacha R, Abdelrahman K. Behaviour of circular SMA-confined reinforced concrete columns subjected to eccentric loading. Eng Struct 2020;215:110443. http://dx.doi.org/10.1016/j.engstruct.2020.110443.

[25] Ben Ftima M, Joder M, Yildiz E. Creep modelling for multi-physical simulation of mass concrete structures using the explicit finite element approach. Eng Struct 2020;212:110538. http://dx.doi.org/10.1016/j.engstruct.2020.110538.

[26] Saeedi A, Shokrieh MM. A novel self-healing composite made of thermally reversible polymer and shape memory alloy reinforcement. J Intell Mater Syst Struct 2019;30(10):1585–93. http://dx.doi.org/10.1177/1045389X19844015.

[27] Cladera A, Weber B, Leinenbach C, Czaderski C, Shahverdi M, Motavalli M. Iron-based shape memory alloys for civil engineering structures: An overview. Constr Build Mater 2014;63:281–93. http://dx.doi.org/10.1016/j.conbuildmat.2014.04.032.

[28] Bagwell S, Ledger PD, Gil AJ, Mallett M, Kruip M. A linearised hp -finite element framework for acousto-magneto-mechanical coupling in axisymmetric MRI scanners. Internat J Numer Methods Engrg 2017;112(10):1323–52. http://dx.doi.org/10.1002/nme.5559.

[29] Yan S, Wu Y, Zhao H, Guo H. Advanced modeling and simulation methods for multiphysics and multiscale problems. Int J Antennas Propag 2017;2017:1–2. http://dx.doi.org/10.1155/2017/3051476.

[30] De Bona F, Mocera F, Srnec Novak J. Material modeling in multiphysics simulation. Metals 2024;14(3):296. http://dx.doi.org/10.3390/met14030296.

[31] Liu Z. Multiphysics in porous materials. Springer International Publishing, Cham; 2018, http://dx.doi.org/10.1007/978-3-319-93028-2_1.

[32] Li H, Dunne D, Kennon N. Factors influencing shape memory effect and phase transformation behaviour of Fe–Mn–Si based shape memory alloys. Mater Sci Eng A 1999;273–275:517–23. http://dx.doi.org/10.1016/S0921-5093(99)00391-3.

[33] Shahverdi M, Michels J, Czaderski C, Motavalli M. Iron-based shape memory alloy strips for strengthening RC members: Material behavior and characterization. Constr Build Mater 2018;173:586–99. http://dx.doi.org/10.1016/j.conbuildmat.2018.04.057.

[34] Shahverdi M, Czaderski C, Annen P, Motavalli M. Strengthening of RC beams by iron-based shape memory alloy bars embedded in a shotcrete layer. Eng Struct 2016;117:263–73. http://dx.doi.org/10.1016/j.engstruct.2016.03.023.

[35] Michels J, Shahverdi M, Czaderski C. Flexural strengthening of structural concrete with iron-based shape memory alloy strips. Struct Concr 2018;19(3):876–91. http://dx.doi.org/10.1002/suco.201700120.

[36] Czaderski C, Shahverdi M, Michels J. Iron based shape memory alloys as shear reinforcement for bridge girders. Constr Build Mater 2021;274:121793. http://dx.doi.org/10.1016/j.conbuildmat.2020.121793.

[37] Tabrizikahou A, Kuczma M, Czaderski C, Shahverdi M. From experimental testing to computational modeling: A review of shape memory alloy fiber-reinforced concrete composites. Composites B 2024;281:111530. http://dx.doi.org/10.1016/j.compositesb.2024.111530.

[38] Keyes DE, McInnes LC, Woodward C, Gropp W, Myra E, Pernice M, Bell J, Brown J, Clo A, Connors J, Constantinescu E, Estep D, Evans K, Farhat C, Hakim A, Hammond G, Hansen G, Hill J, Isaac T, Jiao X, Jordan K, Kaushik D, Kaxiras E, Koniges A, Lee K, Lott A, Lu Q, Magerlein J, Maxwell R, McCourt M, Mehl M, Pawlowski R, Randles AP, Reynolds D, Rivière B, Rüde U, Scheibe T, Shadid J, Sheehan B, Shephard M, Siegel A, Smith B, Tang X, Wilson C, Wohlmuth B. Multiphysics simulations. Int J High Perform Comput Appl 2013;27(1):4–83. http://dx.doi.org/10.1177/1094342012468181.

[39] Dickinson EJ, Ekström H, Fontes E. COMSOL multiphysics®: Finite element software for electrochemical analysis. A mini-review. Electrochem Commun 2014;40:71–4. http://dx.doi.org/10.1016/j.elecom.2013.12.020.

[40] Vajdi M, Sadegh Moghanlou F, Sharifianjazi F, Shahedi Asl M, Shokouhimehr M. A review on the comsol multiphysics studies of heat transfer in advanced ceramics. J Compos Compd 2020;2(1):35–44. http://dx.doi.org/10.29252/jcc.2.1.5.

[41] Simone F, Rizzello G, Seelecke S. A finite element framework for a shape memory alloy actuated finger. J Intell Mater Syst Struct 2019;30(14):2052–64. http://dx.doi.org/10.1177/1045389X19861787.

[42] Seelecke S, Müller I. Shape memory alloy actuators in smart structures: Modeling and simulation. Appl Mech Rev 2004;57(1):23–46. http://dx.doi.org/10.1115/1.1584064.

[43] Davis A, Mirsayar M, Hartl D. A novel structural health monitoring approach in concrete structures using embedded magnetic shape memory alloy components. Constr Build Mater 2021;311:125212. http://dx.doi.org/10.1016/j.conbuildmat.2021.125212.

[44] Karna P, Prabu SSM, Karthikeyan S, Mithun R, Jayachandran S, Resnina N, Belyaev S, Palani I. Investigations on laser actuation and life cycle characteristics of NiTi shape memory alloy bimorph for non-contact functional applications. Sensors Actuators A 2021;321:112411. http://dx.doi.org/10.1016/j.sna.2020.112411.

[45] Rodinò S, Maletta C. Multiphysics modeling and optimization of an innovative shape memory alloy-polymer active composite. Polymer 2024;307:127316. http://dx.doi.org/10.1016/j.polymer.2024.127316.

[46] Saeedi A, Kwon H, Soni P, Dillenburger B, Shahverdi M. Design and multiphysical modeling of SMA-driven bi-stable structures with efficient energy consumption. Eng Struct 2024;314:118367. http://dx.doi.org/10.1016/j.engstruct.2024.118367.

[47] Zheng Y, Dong Z, Liu Z, Wu G, Zhu H, Wei Y. An activation guideline for the resistive heating process of iron-based shape memory alloy embedded in concrete. Structures 2024;68:107079. http://dx.doi.org/10.1016/j.istruc.2024.107079, URL https://linkinghub.elsevier.com/retrieve/pii/S2352012424012311.

[48] Lagoudas D, Hartl D, Chemisky Y, Machado L, Popov P. Constitutive model for the numerical analysis of phase transformation in polycrystalline shape memory alloys. Int J Plast 2012;32–33:155–83. http://dx.doi.org/10.1016/j.ijplas.2011.10.009.

[49] Czaderski C, Shahverdi M, Brönnimann R, Leinenbach C, Motavalli M. Feasibility of iron-based shape memory alloy strips for prestressed strengthening of concrete structures. Constr Build Mater 2014;56:94–105. http://dx.doi.org/10.1016/j.conbuildmat.2014.01.069.

[50] Stocker F. Semester project report: study the behavior of concrete bars prestressed by embedded fe-SMA. ETH Zürich, Institute of Structural Engineering and EMPA, Structural Engineering; 2014.

[51] Lagoudas DC. shape memory alloys. Springer US, Boston, MA; 2008, http://dx.doi.org/10.1007/978-0-387-47685-8.

[52] Lee W, Weber B, Feltrin G, Czaderski C, Motavalli M, Leinenbach C. Phase transformation behavior under uniaxial deformation of an Fe–Mn–Si–Cr–Ni–VC shape memory alloy. Mater Sci Eng A 2013;581:1–7. http://dx.doi.org/10.1016/j.msea.2013.06.002.

[53] Ottosen NS. A failure criterion for concrete. J Eng Mech Div 1977;103(4):527–35. http://dx.doi.org/10.1061/JMCEA3.0002248.

[54] Chen W-F. Plasticity in reinforced concrete. J. Ross Publishing, Plantation, FL; 2007.